# The Use of Silica Coated MnO Nanoparticles to Control MRI Relaxivity in Response to Specific Physiological Changes

Yi-Cheng Lee [a], Der-Yow Chen [b], Stephen J. Dodd [b], Nadia Bouraoud [b], Alan P. Koretsky [b,**], Kannan M. Krishnan [a,*]

[a] Department of Materials Science and Engineering, University of Washington, Seattle, WA 98195, USA
[b] NINDS, National Institutes of Health, Bethesda, MD 20892, USA

## ARTICLE INFO

## ABSTRACT

MnO nanoparticles have been tested to engineer a delayed increase in MRI $T_1$ relaxivity caused by cellular uptake via endocytosis into acidic compartments. Various coatings on core–shell structured MnO nanoparticles were tested for those that had the lowest $T_1$ relaxivity at pH 7.4, a pH where MnO does not dissolve into $Mn^{2+}$ ions. The rate of dissolution and release of $Mn^{2+}$ of the different coated MnO particles as well as changes in $T_1$ relaxivity were measured at pH 5, a pH routinely obtained in the endosomal-lysosomal pathway. Of a number of coatings, silica coated MnO ($MnO@SiO_2$) had the lowest relaxivity at pH 7.4 ($0.29$ $mM^{-1}$ $sec^{-1}$). About one third of the MnO dissolved within 20 min and the $T_1$ relaxivity increased to that of free $Mn^{2+}$ ($6.10$ $mM^{-1}$ $sec^{-1}$) after three days at pH 5. MRI of $MnO@SiO_2$ particles injected into the rat brain showed time-dependent signal changes consistent with the in vitro rates. Thalamocortical tract-tracing could be observed due to the released $Mn^{2+}$. Intravenous infusion of $MnO@SiO_2$ particles showed little enhancement in any tissue except gallbladder. The gallbladder enhancement was interpreted to be due to endocytosis by liver cells and excretion of $Mn^{2+}$ ions into the gallbladder. The $MnO@SiO_2$ core–shell nanoparticles show the best potential for delaying the release of MRI contrast until endocytosis into low pH compartments activate MRI contrast. The delayed enhancement may have benefits for targeting MRI contrast to specific cells and surface receptors that are known to be recycled by endocytosis.

© 2012 Elsevier Ltd. All rights reserved.

## 1. Introduction

Magnetic resonance imaging has been widely used for providing high resolution anatomical imaging of animals and humans but is less sensitive than radiotracer imaging modalities for molecular imaging applications. Nonetheless, various contrast agents have been developed for cellular and molecular imaging using MRI [1,2]. With most of these agents, MRI relaxivity do not change and often there are problems distinguishing non-specific effects from specific effects. New contrast agents, with the capability of altering MRI relaxivity in response to specific physiological changes, such as tissue/cellular variations in pH, redox state, oxygenation, or metabolite levels, are gaining more attention. For example, $Gd^{3+}$-based MRI contrast agents where water access is blocked and unblocked either with binding of small molecules or via enzymatic cleavage have been developed [3,4]. New paramagnetic chelates have been designed that are very sensitive to altered water exchange that can be altered by binding of molecules such as glucose [5]. Advanced protein engineering techniques are also being applied to make MRI based biosensors [6]. Small iron oxide particulates [7] have also been developed that serve as a platform for magnetic resonance $T_2$ relaxation switches [8–10]. None of these switchable agents have found widespread use due to the relatively small dynamic range of relaxivity changes and the problem of delivering these agents even in animal models.

Manganese enhanced MRI (MEMRI) has found widespread use in MRI [11]. $Mn^{2+}$ ions can visualize anatomical structures of the brain, neuronal activity, and connections between brain regions [12,13]. MEMRI has also been shown to be useful in imaging cardiac function and pancreatic function [14,15]. There has been interest in engineering Mn nanoparticles for MRI [16]. Recently, it has been shown that MRI contrast from certain Mn particles that have very low MRI $T_1$ relaxivity can be increased dramatically due to dissolution of the particles and release of $Mn^{2+}$ ions in the low pH environment found in the mammalian endosomal-lysosomal

pathway [17,18]. $Mn^{2+}$ can leave the endosomal-lysosomal pathway to fill the entire cell leading to a much larger volume distribution of the contrast agent [17,19]. This opens the possibility of getting a large, specific, increase in MRI contrast upon cellular uptake. A limitation is that the particles have not been optimized for low relaxivity at normal pH and optimal dissolution rate.

It is well-known that transition metal oxides, such as MnO, dissolve in acidic solutions leading to the release of $Mn^{2+}$ ions. Therefore, MnO nanoparticles were tested with different coating materials, creating core–shell morphologies, to test their effect on controlling MRI $T_1$ relaxivity and dissolution rate at pH 5. The goal was to have low relaxivity at pH 7.4 and a slow dissolution rate at pH 5. The slow dissolution rate opens the possibility of imaging only those particles that have been taken up into the endosomal–lysosomal pathway, enabling other particles to be cleared from blood and non-specific extracellular binding sites. This in turn is expected to lead to more specific imaging of cellular uptake processes occurring in vivo. In the present work, five different coatings on MnO nanocrystals were tested in vitro to study the release rate of the $Mn^{2+}$ ions and change in relaxivity at pH 7.4 compared to pH 5. Silica coated MnO was selected and applied for in vivo experiments. Particles were injected directly into the cortex of the brain and intravenously into rodents. The system of neuronal thalamocortical connectivity in a rodent model is well established [13]. Particles injected into the thalamus were expected to increase MRI $T_1$ contrast on a time scale similar to the dissolution rate measured in vitro. Furthermore, $Mn^{2+}$ tracing to thalamus should also be detected after injection of particles into the brain cortex. The latter part, intravenous infusion of the MnO@SiO$_2$ nanoparticles into mice, was performed to identify biodistribution of nanoparticles and MRI contrast enhancement after cellular uptake process. In both in vivo studies, silica coated iron oxide particles were utilized as control to investigate whether MRI contrast enhancement resulted from transport of particles or $Mn^{2+}$. The enhancement in specific tissues indicates that particles will be excellent for visualizing particle uptake by endocytic cells such as macrophages. The lack of contrast in other tissues indicates that these particles may be excellent to be used as molecular targeting agents.

## 2. Materials and methods

### 2.1. Synthesis of MnO nanocrystals

To develop an MRI contrast agent that is activated by cell uptake into low pH compartments, the first requirement is for the contrast agent to exhibit a low relaxation rate in neutral pH (in normal body compartments and/or fluid) and a higher relaxation rate in lower pH. A second design feature for the present studies was to have delayed activation when transferred to a low pH environment to help potentially increase the specificity for MRI detection. Inorganic manganese oxides are known to be insoluble at neutral pH but their dissolution can be accelerated by the presence of excess protons, i.e. acidic solutions. Using MnO nanoparticles as the $Mn^{2+}$ source and coating them with five different materials, to create core-shells, we tested the dissolution rate of $Mn^{2+}$ from the nanoparticles. Coatings were chosen to see how efficiently different types of materials (small molecules, polymers, and inorganic materials) would affect the relaxivity change. Mercaptosuccinic acid (MSA), a representative small molecule; Pluronic PF127, a widely used polymeric molecule in drug delivery applications [20]; PMAO and PMAO-PEG, both proven to provide high quantum yield of quantum dots after phase transferring, and SiO$_2$, a popular inorganic coating material were used. All of them were tested for their ability to retard the particles from dissolving at pH 5 and slowly release $Mn^{2+}$ ions over time.

Highly monodisperse, single-phase, MnO nanocrystals (NCs), ~10 nm in diameter, were prepared by chemical routes and their structure and magnetic properties were extensively characterized [21,22]. Monodispersed MnO nanoparticles were synthesized by thermal decomposition of a Mn-oleate complex in an organic solvent [23]. The Mn-oleate complex was prepared by mixing 0.2 g of $Mn_2(CO)_{10}$ in 2 mL of oleylamine at 100 °C. The complex solution was cooled to room temperature and then 10 mL of trioctylphosphine was added. For the growth of nanocrystals, the solution mixture was heated up to 280 °C under argon atmosphere and kept under vigorous stirring for 1 h. The reactants were then cooled to room temperature and the nanoparticles were obtained by adding ethanol, followed by centrifugation. They were then re-dispersed in non-polar solvents such as hexane or toluene.

### 2.2. Transferring MnO particles into aqueous solution with five different coatings

Nanoparticles synthesized in non-polar solvents have narrow size distributions but are not biocompatible. Hence, the MnO nanocrystals were coated with amphiphilic molecules to help disperse them in aqueous solutions for biomedical applications. Mercaptosuccinic acid (MSA), poly(maleic anhydride-alt-1-octadecene) (PMAO), Pluronic F-127 (PF127), PMAO-PEG and SiO$_2$ were then used, respectively, to transfer native hydrophobic particles to aqueous solutions. The method of producing MnO nanoparticles with five different coatings are as follows:

a) MnO@MSA: MnO nanoparticles (20 mg) in 4 mL chloroform and mercaptosuccinic acid (MSA) (30 mg) in 4 mL dimethyl sulfoxide (DMSO) were loaded in a small vial. The mixture was stirred for 20 h. The particles were washed with ethanol and collected by centrifugation. These particles were re-dispersed in buffer solutions and were ready to be used for in vivo experiments.

b) MnO@PF127: MnO nanoparticles (20 mg) and pluronic F127 (80 mg) were mixed with 4 mL chloroform in a small vial. The mixture was stirred for 20 h. Then all the solvents were evaporated and particles were re-dispersed in buffer solutions.

c) MnO@PMAO: A solution of 100 mg poly(maleic anhydride-alt-1-octadecene) in 2 mL CHCl$_3$ and a solution of 15 mg MnO nanoparticles in 3 mL CHCl$_3$ were mixed and stirred for 2 h at room temperature. 10 mg 1,10-diaminodecane in 1 mL CHCl$_3$ was then added to crosslink the polymer shell that had formed around each particle. The mixed solution was sonicated for 10 min and stirred for 20 h. Followed by evaporating the solvent, a brown solid was obtained and re-dispersed in TAE buffer solutions.

d) MnO@PMAO-PEG: A solution of 85 mg PMAO-PEG in 2 mL CHCl$_3$ and a solution of 15 mg MnO nanoparticles in 3 mL CHCl$_3$ were mixed and stirred for 2 h at room temperature. The solvent was then evaporated and the solid obtained was re-dispersed in TAE buffer solutions. PMAO-PEG was obtained as follows. 2 g poly(maleic anhydride-alt-1-octadecene), 0.6 g poly ethylene glycol methyl ether and 0.3 mL $H_2SO_4$ were mixed in 20 mL Acetone solution and refluxing at 57 OC for 24 h. Followed by adding de-ionized water, white PMAO-PEG was obtained and ready for the above reaction.

e) MnO@SiO$_2$: Igepal CO-520 (0.54 mmol) dispersed in 4.5 mL cyclohexane by sonication and MnO nanoparticles (0.4 mg) in 0.4 mL cyclohexane were mixed in a small vial. Then ammonium hydroxide (0.04 mL) was added to the mixture and stirred for 2 min. Subsequently, tetraethyl orthosilicate (TEOS) (0.03 mL) was added and the reaction was continued for 48 h. The particles were precipitated with excess hexane and collected by centrifugation. The total size of particles was ~20 nm in diameter with 10 nm core and 5 nm shell thickness as determined by transmission electron microscopy (TEM).

### 2.3. MRI parameters for in vitro relaxivity measurements

$T_1$ relaxation times of the various-coated MnO core–shell nanoparticles, dispersed in water and prepared in 1 mL syringes with varying concentrations, were measured on an 11.7T/31 cm horizontal bore magnet (Magnex Scientific Ltd., Abingdon, UK), which was equipped with a 12 cm gradient/shim set (Resonance Research Inc., Billerica, MA, USA) and interfaced to a Bruker Avance console (Bruker BioSpin, Billerica, MA, USA). A 90 mm volume coil was used for transmit and receive. A $T_1$ saturation recovery sequence (TR = 200, 642.6, 1211.7, 2010.4, 3360.2, 10,000 ms; TE = 8.63 ms) was used to measure $T_1$. The images were fitted into a 3-parameter function to calculate $T_1$ values using Bruker TopSpin built-in analysis program. The specific relaxivities ($r_1$) of the MnO nanoparticles were measured as follows. Each sample was prepared in five different concentrations, and $T_1$ values were measured for each concentration, which were then used for $r_1$ calculations, respectively. Relaxivity was determined from the slope of concentration-dependent $T_1$ changes. The Mn concentrations were based on the molar concentration of manganese atom measured by ICPMS.

#### 2.3.1. In vivo observation of increasing contrast enhancement in the rat brain with injection of MnO@SiO$_2$ core–shell nanoparticles

MnO@SiO$_2$ core–shell nanoparticles were injected into the thalamus to observe the local contrast enhancement with time. It was also injected into the cortex (S1) to test their capability of being neuronal tract-tracing agents. Silica coated Fe$_3$O$_4$ was used as a control for independently verifying the location of particles.

### 2.4. Synthesis of SiO$_2$ coated Fe$_3$O$_4$ (Fe$_3$O$_4$@SiO$_2$) core–shell nanoparticles

As a control for the properties of MnO@SiO$_2$, silica coated iron oxide particles (Fe$_3$O$_4$@SiO$_2$) were synthesized. Igepal CO-520 (10 mL) dispersed in 170 mL cyclohexane by sonication and Fe$_3$O$_4$ nanoparticles [24] (52 mg) in 10 mL cyclohexane were mixed in a flask. Then ammonium hydroxide (1.3 mL) was added to the mixture and stirred for 2 min. Subsequently, tetraethyl orthosilicate (TEOS) (0.7 mL) was added and the reaction was continued for 48 h. The particles were precipitated with excess hexane and collected by centrifugation.

### 2.5. Animal procedure for brain injections of nanoparticles

All animal work was performed according to the guidelines of the Animal Care and Use Committee and the Animal Health and Care Section of the National Institute

of Neurological Disorders and Stroke, National Institutes of Health (Bethesda, MD, USA). A total of six adult male Sprague−Dawley rats (250−300 g) were used in this study. For thalamic injections, six rats received 100 nL of 16.8 mM MnO@SiO₂ nanoparticle solution and aqueous MnCl₂ (Sigma−Aldrich, St. Louis, MO, USA), which was buffered with Bicine (Sigma−Aldrich, St. Louis, MO, USA) and brought to physiological pH with NaOH. Nanoparticle solution was injected into the right hemisphere (Anterior/Posterior (AP) −3.0 mm, Medial/Lateral (ML) 2.5 mm, and Depth/Ventral (DV) 6.5 mm) and aqueous MnCl₂ was injected into the left hemisphere (AP −3.0 mm, ML −2.5 mm, and DV 6.5 mm). For cortical injections, four rats received 400 nL of 16.8 mM MnO@SiO₂ nanoparticle solution. Injections were made into the right S1 cortex in the forepaw area (AP 0.0 mm, ML 3.8 mm, and DV 3.2 mm). All stereotactic coordinates were determined according to the Paxinos and Watson atlas [25]. MRI was performed immediately after injection. For stereotactic injections, animals were initially anesthetized by 5% isoflurane (3:3:1 air: nitrogen: oxygen mixture), positioned in a stereotactic frame (Stoelting) and kept on 2−3% isoflurane during the surgery. A small burr hole was drilled after exposing the skull. A Hamilton syringe was placed at the proper coordinates in the stereotactic frame. Injections were performed slowly over 5 min and the syringe was slowly removed. The burr hole was sealed with bone wax and the muscle sutured closed. MRI was performed right after stereotactic injections to make sure solutions were delivered to the proper sites and then at varying times after injections. For MRI scans, rats were initially anesthetized with 5% isoflurane and placed in a custom made plastic stereotactic holder. The anesthesia was maintained at 1−2% using a nose cone and rectal temperature was maintained at 37 ± 1 °C by a heated water bath. After surgery and in between scans, animals were allowed to recover and were free to roam within their cages. No abnormalities were observed after injection in all the rats.

### 2.6. MRI parameters for brain imaging

Brain images were acquired on an 11.7T/31 cm horizontal bore magnet (Magnex Scientific Ltd., Abingdon, UK), which was equipped with a 12 cm gradient/shim set (Resonance Research Inc., Billerica, MA, USA) and interfaced to a Bruker Avance console (Bruker BioSpin, Billerica, MA, USA). A 90 mm volume coil was used for transmit and surface coil was used as receive. A Magnetization Prepared Rapid Gradient Echo (MP-RAGE) sequence was used. Sixteen coronal slices with FOV = 2.56 × 2.56 cm, matrix 256 × 256, thickness = 0.5 mm (TR = 4000 ms, Echo TR/TE = 15/5 ms, TI = 1000 ms, number of segments = 4, Averages = 8) were used to cover the area of interest at 100 μm in-plane resolution in 34 min. Fast Low Angle SHot Magnetic Resonance Imaging (FLASH) sequence was used to obtain $T_2$*-weighted images. Sixteen coronal slices with FOV = 2.56 × 2.56 cm, matrix 256 × 256, thickness = 0.5 mm (TR = 25 ms, TE = 12 ms, averages = 2) were used to cover the area of interest at 100 μm in-plane resolution in 34 min.

### 2.7. MRI studies of MnO@SiO₂ core−shell nanoparticles infused intravenously via the mouse tail vein

To obtain an idea of the biodistribution of MnO@SiO₂ in the mouse body when the particles are infused through the tail vein, $T_1$-weighted imaging was used. A total of four adult female FVB mice (25−30 g) were used in this study. Four mice received 35 μL of 16.8 mM MnO@SiO₂ nanoparticle solution through tail vein infusion. MRI was performed immediately after infusion. For tail vein injections, animals were initially anesthetized by 4% isoflurane (3:3:2 air: nitrogen: oxygen mixture), and kept on 2−3% isoflurane during the infusions. Injections were performed slowly over 2.6 min. MRI was performed right after and at varying times after injections. For MRI scans, mice were placed in a custom made plastic holder. The anesthesia was maintained at 1−2% using a nose cone and rectal temperature was maintained at 37 ± 1 °C by a heated water bath. No abnormalities were observed after injection in all the mice. MRI for the tail vein injection were acquired on a 7T/21 cm horizontal bore Bruker Biospec System. A Fast Low Angle SHot (FLASH) sequence synchronized to respiratory motion was applied to acquire images. The echo time (TE) was 2.559 msec, and repetition time (TR) was approximately 105 msec and the excitation flip angle was 60° to set $T_1$-weighting. Each set consisted of 16 slices with no gap and a FOV = 3.84 × 2.56 × 1.2 cm, matrix 128 × 192 × 16. To obtain $T_2$*-weighted images for experiments where SiO₂ coated iron oxide particles were injected, the echo time (TE) was 6 msec, and repetition time (TR) was approximately 290.4 msec and the excitation flip angle was 30°. Each set consisted of 16 slices and a FOV = 3.84 × 2.56 cm, matrix 384 × 256.

## 3. Results

### 3.1. Relaxivity profiles of MnO core−shell nanoparticles with five different coatings

Table 1 shows relaxivities of core−shell nanoparticles coated with different materials in PBS buffer solutions (pH 7.4) and acetate buffer solutions at pH 5.0. MnO@SiO₂ in pH 7.4 had the smallest relaxivity ($r_1 = 0.29$ mM$^{-1}$ s$^{-1}$) amongst all the samples. This means that SiO₂

**Table 1**
Relaxivities (s$^{-1}$mM$^{-1}$) of nanoparticles as a function of pH and time.

| Capping on MnO | $r_1$ pH 7.4 20 min. | $r_1$ pH 5.0 20 min. | $r_1$ pH 5.0 3 days |
|---|---|---|---|
| SiO₂ | 0.29 | 2.60 | 6.10 |
| PMAO-PEG | 1.79 | 3.57 | 6.31 |
| Pluronic PF127 | 1.91 | 6.59 | 6.59 |
| PMAO | 2.42 | 3.38 | 6.39 |
| MSA | 2.55 | 6.94 | 6.91 |

provided the best shell for slowing the release of Mn$^{2+}$ from the nanoparticles at neutral pH as well as blocking any relaxivity effects from the surface of the particles. On the other hand, MnO@MSA in pH 7.4 had the largest value ($r_1 = 2.55$ mM$^{-1}$ s$^{-1}$). When the particles were immersed in acetate buffer solutions (pH 5.0), relaxivities of MnO@MSA and MnO@PF127 increased to 6.94 mM$^{-1}$ s$^{-1}$ and 6.59 mM$^{-1}$ s$^{-1}$, respectively, in 20 min. MnO@SiO₂ still had the smallest value ($r_1 = 2.60$ mM$^{-1}$ s$^{-1}$) at 20 min indicating that roughly one third of the MnO had dissolved. After three days of immersions of particles, all coatings showed that they were almost totally dissolved as the $r_1$ reached a value similar to that of MnCl₂ ($r_1 = 6.22$ mM$^{-1}$ s$^{-1}$) in pH 5.0 buffer solutions.

The detailed time-dependent relaxivity measurements of MnO@SiO₂ nanoparticles at pH 5.0 in acetate buffer solution is shown in Fig. 1. Almost half the total amount of Mn$^{2+}$ ions in the particles was dissolved within the first 5 h, but the relaxivity changes slowed down after 10 h. Relaxivity values increased from 2.44 s$^{-1}$ mM$^{-1}$ at 53 min to 6.1 s$^{-1}$ mM$^{-1}$ after 75 h. The final relaxivity approached that of MnCl₂ indicating that the particles had almost completely dissolved. The results also imply that the silica shell was porous in structure enabling the MnO to dissolve at low pH consistent with reports in the literature [26]. MnO@SiO₂ showed the most stability in neutral pH and the slowest dissolution rate when immersed in acetate buffer solutions. Therefore, it was selected for further in vivo experiments of brain and body imaging using rat and mice models, respectively.

### 3.2. In vivo time-dependent $T_1$ enhancement with MnO@SiO₂ after injection into the brain

Fig. 2 compares MRI of the brain after injection of MnCl₂ (right side) and MnO@SiO₂ (left side) into the respective thalamic areas.
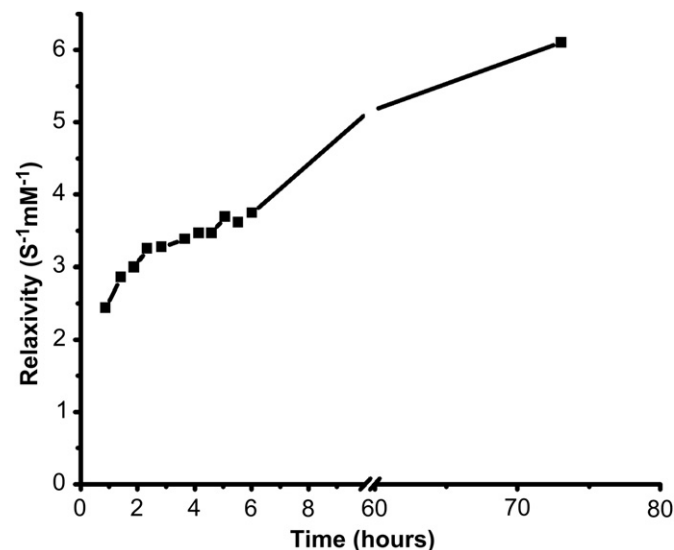


**Fig. 1.** Time-dependent relaxivity of MnO@SiO₂ nanoparticles soaking in pH 5.0 buffer solutions.

The time course of images was from 1 h (a) up to 6 h (d) post injection. The same molar concentration of Mn was injected, however, the positive contrast at the site of MnCl$_2$ injection (right sides of images) was most enhanced in the first image taken immediately after injection and decreased slightly with time most likely due to washout or transport of the Mn$^{2+}$ ions. In contrast, the signal intensity at the injection site of MnO@SiO$_2$ particles (left side in images) increased with time, as shown in Fig. 2(e), consistent with the slow dissolution rate measured *in vitro*. The increased signal percentage was calculated as the following equation: {[signal(each time point)−signal(2 h)]/signal(2 h)}*100%.

The increase in contrast after injection of MnO@SiO$_2$ particles is attributed to dissolution of the particles to release Mn$^{2+}$. Mn$^{2+}$ is known to be an effective neuronal tracing agent, whereas nanoparticles have not been shown to be effective neural tracing agents. Therefore, the suitability of MnO@SiO$_2$ particles to be source of Mn$^{2+}$ for neuronal tract-tracing by MRI was tested. For the tracing experiments the solution of particles was injected into the somatosensory cortex (S1). Fig. 3(a) shows the results 20−24 h after injection of the particles. The right panel of Fig. 3(a) shows the MRI slice that includes the cortical injection site (arrow) which is brightly enhanced since this is a time when all of the particles are expected to be dissolved. The left panel of Fig. 3(a) shows the MRI slice that includes the thalamus. A T$_1$ enhanced signal in the thalamus could be readily detected, confirming that thalamocortical tract-tracing can be accomplished from Mn$^{2+}$ using the MnO@SiO$_2$ nanoparticles.

To test that the tract-tracing was mainly due to the movement of Mn$^{2+}$ through the thalamocortical neuronal pathway rather that the SiO$_2$ coating a control experiment was performed with SiO$_2$ coated iron oxide particles. Fe$_3$O$_4$@SiO$_2$ core−shell nanoparticles of comparable size to the MnO@SiO$_2$ with the magnetite core ∼9 nm in diameter and the silica shell ∼5 nm in thickness; i.e. the total particle size is ∼20 nm in diameter. Fig. 3(b) shows T$_2$*-weighted images to detect the iron oxide. The panel on the right of Fig. 3(b) shows that the cortical injection site had low signal (dark contrast) due to injection of the iron oxide into the cortex. The panel on the right of Fig. 3(b) shows the MRI from the slice that contains the thalamus. No contrast change in the region of the thalamus was observed 20 h post injection. The signal intensity at both hemispheres of thalamus showed no significant difference.

### 3.3. MRI contrast from MnO@SiO$_2$ nanoparticles infused into mice through the tail vein

Studies were conducted injecting MnO@SiO$_2$ particles into the tail vein of mice and imaged with T$_1$-weighted MRI. The aim was to measure the enhancement caused by the particles in various organs of the mouse. FVB mice (26.7−28.6 g of body weight) were injected with enough particles to deliver 1.2 μg manganese/gm body weight and images were acquired for up to 2 h after infusion. The half-life of the particles circulation in the blood was determined. Blood samples were taken at different time intervals from three different mice to determine Mn concentrations using ICPMS measurements. Fig. 4 shows the time course of decay in Mn after tail vein infusion. Each point in Fig. 4 represents one blood sample and the time course was generated from all three mice. The results show that the blood half-life of MnO@SiO$_2$ particles was ∼10 min at the concentration of 1.2 μg Mn infusion per gram of mice body weight.

The time course of T$_1$ MRI enhancement of different organs were determined after IV infusion of MnO@SiO$_2$. Fig. 5(a) shows images from a slice that contained gallbladder (left image), liver (middle image) and kidney (right image). These images were taken 116 min after injection of the MnO@SiO$_2$ particles. The gallbladder can be readily detected because of the large enhancement. Time course of signal intensity changes are shown for the gallbladder, liver, and kidney in Fig. 5(b). All intensities were normalized to the pre-infusion values. The signal intensity in the gallbladder started to increase after 20 min post-infusion and reached its saturation value at 90 min. Gallbladder signal increased about two fold. There was a smaller increase in the liver and kidney where signal increased about 66%. There were even smaller enhancements in other organs such as heart (data not shown). In all cases the contrast did not start to increase until 10 min after infusion a time when blood particle concentration was rapidly falling. This is consistent with the particles being taken up and contrast turned on as the particles dissolve.

The gallbladder enhancement demonstrates that the contrast was due to dissolved Mn$^{2+}$. The gallbladder began to enhance 20 min post-infusion of particles, a time when blood particle levels were low. Furthermore, there is no known pathway for nanoparticles to enter the gallbladder. To test if SiO$_2$ coated particles can enter the gallbladder, Fe$_3$O$_4$@SiO$_2$ nanoparticles were used and infused through tail vein of mice and monitored with T$_2$-weighted imaging. Fig. 6 shows the T$_2$-weighted images of Fe$_3$O$_4$@SiO$_2$
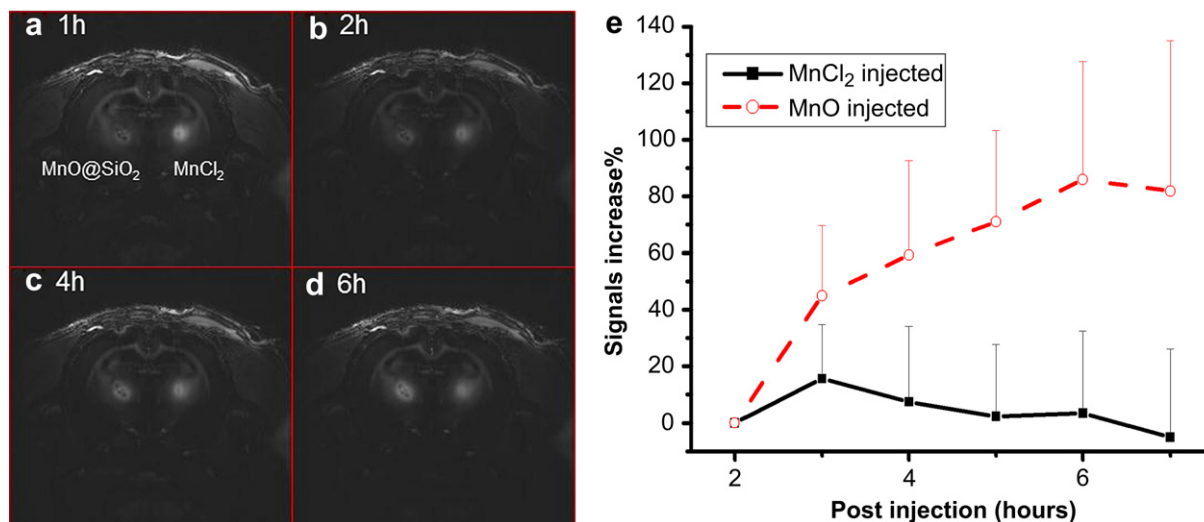


**Fig. 2.** MP-RAGE images of injected MnCl$_2$ and MnO@SiO$_2$ solutions: (a) 1 h, (b) 2 h, (c) 4 h, and (d) 6 h post injection. (e) Time course study of signals increase percentage (average of three rats) at the sites of injected MnCl$_2$ and MnO@SiO$_2$ solutions.
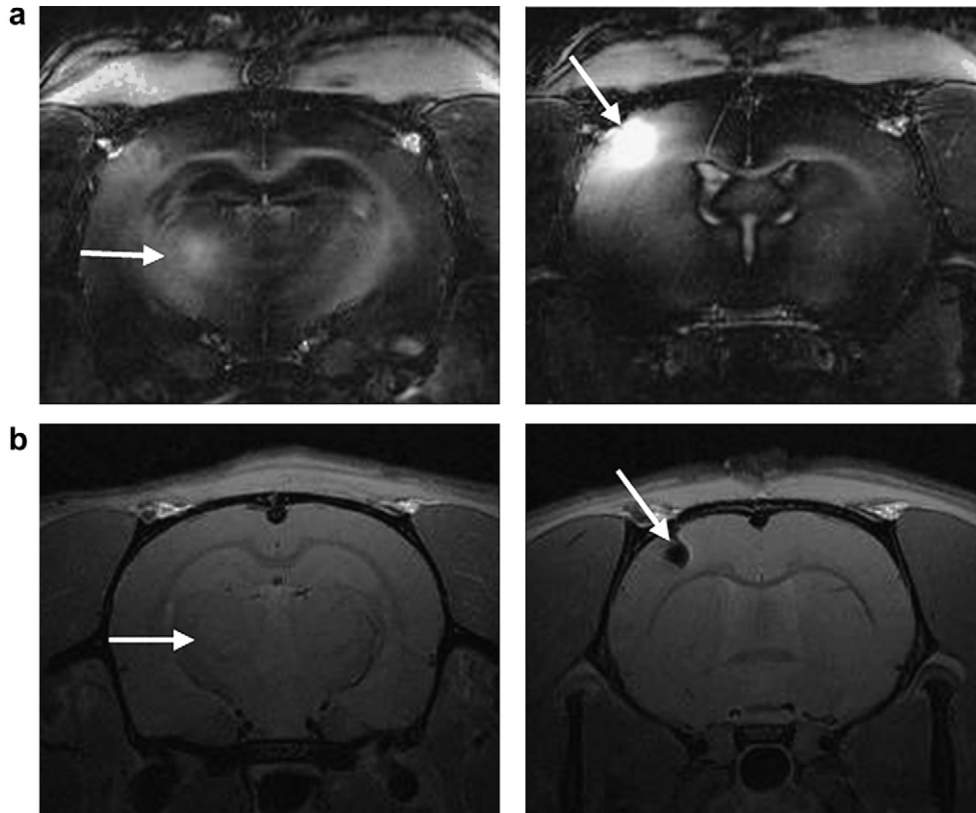
**Fig. 3.** (a) MP-RAGE images of thalamocortical tract-tracing with the injection of MnO@SiO$_2$ nanoparticles at the cortex (S1). The arrow in the left image indicates the enhanced thalamus compared to contra-lateral hemisphere. The arrow in the right image is the injection site. Both images were acquired 24 h after injection was made at the cortex. (b) T$_2$-weighted images of thalamocortical tract-tracing experiment with the injection of Fe$_3$O$_4$@SiO$_2$ nanoparticles in the S1. The left image with an arrow is the thalamus showing no enhancement at 20 h post injection. The right image is the injection site showing clear dark contrast. Both images were acquired 20 h after injection was made at the cortex.

particles before, 6 min and 77 min after tail vein infusion. The arrow indicates the liver. There is a signal drop in liver at 6 min post-infusion (the image in the middle), the contrast gets larger (image on right) at the liver region after 77 min post-infusion (the image on the right). No change in signal of the gallbladder was detected. This indicates that the Fe$_3$O$_4$@SiO$_2$ nanoparticles are transported to the liver in less than 6 min. On the other hand, when
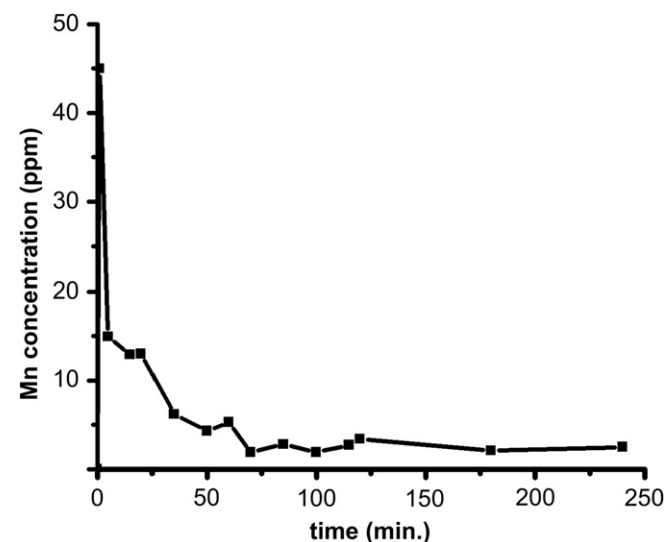


**Fig. 4.** Time-dependent Mn concentration as a function of particle circulation half-life in the mice blood.

MnO@SiO$_2$ particles were infused into the mice tail vein, the positive contrast was enhanced mostly in the gallbladder and was delayed and did not begin until 20 min. Combining the results of using these two types of core–shell nanoparticles, it is likely that the MnO@SiO$_2$ particles are taken up by the liver which is followed by the release of Mn$^{2+}$ and excretion to the gallbladder leading to the enhanced contrast in the gallbladder. The fact that the liver itself did not enhance that much indicates that the transport of Mn$^{2+}$ to the gallbladder was on the order of the rate of dissolution of the particles.

In summary, the gallbladder showed the most enhanced positive T$_1$ contrast when MnO@SiO$_2$ nanoparticles were infused. On the other hand, only the liver showed negative T$_2$ contrast when Fe$_3$O$_4$@SiO$_2$ nanoparticles were infused. Assuming that the MnO@SiO$_2$ particles followed the same pathway as Fe$_3$O$_4$@SiO$_2$, it is likely that the MnO@SiO$_2$ particles are first endocytosed by liver (probably by Kupffer cells) resulting in the release of Mn$^{2+}$ ions and then the Mn$^{2+}$ ions are excreted through bile duct leading to the positive contrast in the gallbladder. There was much less contrast in other organs indicating that if something caused accumulation of particles in these other tissues either due to cell infiltration with higher endocytic capacity such as macrophages or due to targeting the particles with antibodies, that there will be little non-specific background.

## 4. Discussion

The main goal of this work was to develop an MRI contrast agent that has very low relaxivity at normal physiological pH (pH 7.4) but that increases relaxivity after cell uptake by endocytosis and
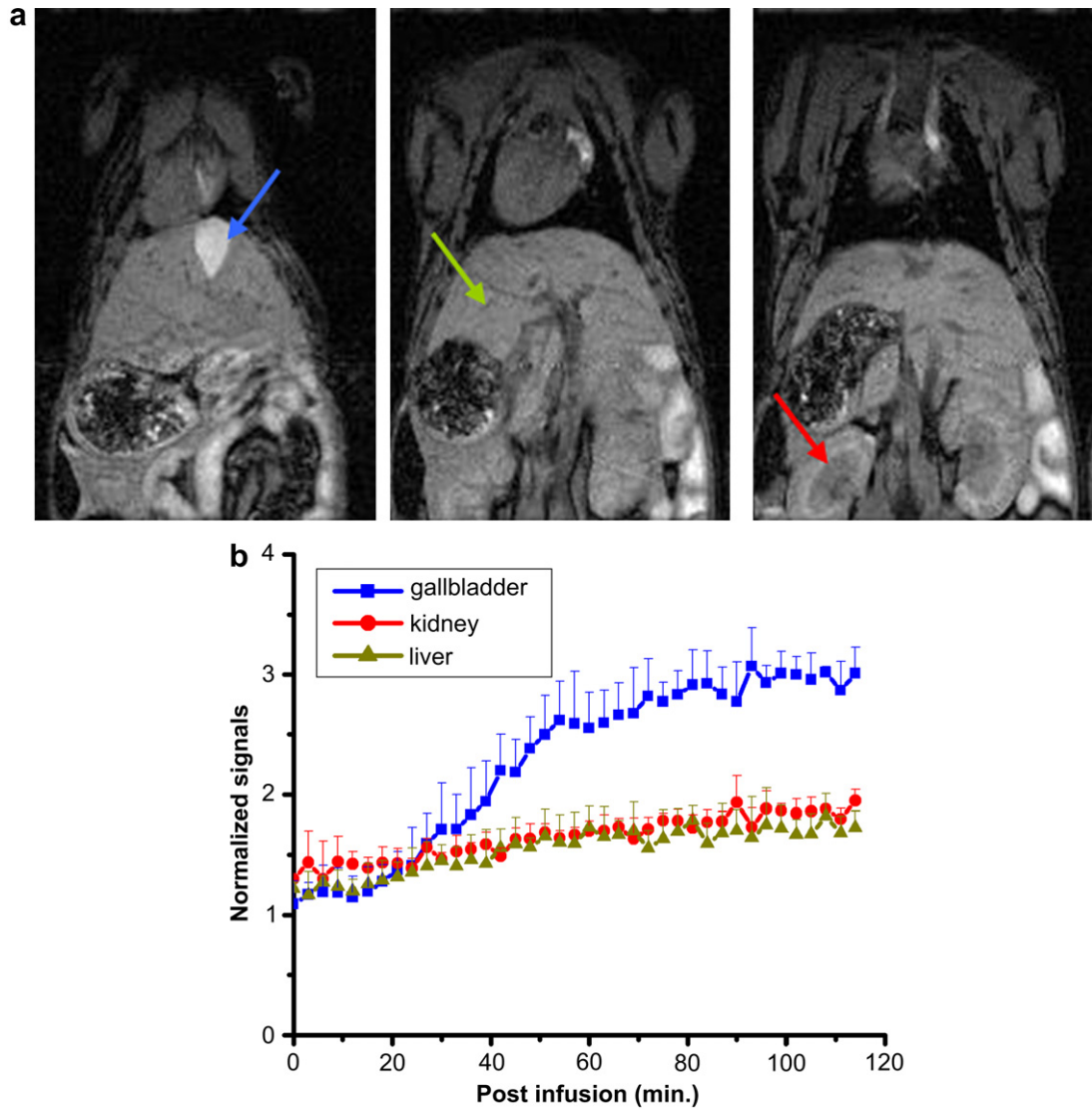
**Fig. 5.** (a) Regions of interest in the gallbladder (on the left), kidney (on the middle) and liver (on the right) acquired 116 min after injection; (b) time course study of the enhanced signal in the gallbladder, kidney and liver after infusions of particles.
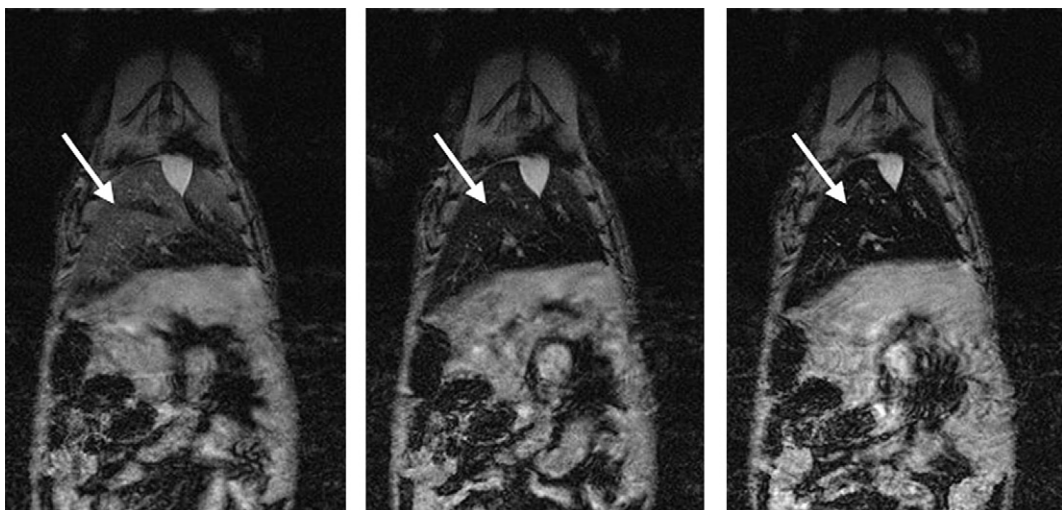


**Fig. 6.** T$_2$-weighted images of pre-infusion (left), 6 min post-infusion (middle) and 77 min post-infusion (right). The arrows indicate the liver.

exposure to low pH (pH 5) in the endosomal-lysosomal pathway. Most molecular imaging applications target imaging agents to receptors on cell surfaces that are internalized by endocytosis into low pH environments. The ability to have the contrast turn on after endocytosis may lead to higher specificity. Similarly there has been a lot of work with iron oxide particles to label macrophages which are highly endocytic cells that uptake the particles into the endosomal–lysosomal pathway. Having a contrast agent that turns on after uptake by these cells may also increase specificity for cell labeling. Having that contrast agent delay enhancement until after agent can clear extracellular spaces and blood could further improve specificity.

Earlier work has demonstrated that MnO and MnCO$_3$ particles have low relaxivity as particles and increase relaxivity at low pH due to dissolution of the particles Mn$^{2+}$ [17,18]. Therefore, the focus of the present work was to determine if MnO nanoparticles with different coatings could be developed with very low relaxivity at pH 7.4 and slow but complete dissolution at pH 5. Slow dissolution is to enable particles to clear from blood and extracellular spaces. Typical half-lifes for nanoparticles range from a few minutes to 45 min [27] which gives a starting target for the time scale that slowing dissolution would be useful. Five different coatings on MnO particles were used, creating a core−shell morphology. These coatings helped with phase transfer of the highly monodisperse nanoparticles from organic solvents to aqueous solutions, but also could be optimized for low relaxivity at pH 7.4 and slowing the release of Mn$^{2+}$ at low pH of the lysosomal system.

The relaxivity measurements for the five different coatings on MnO nanoparticles show that all of them dissolved at low pH. There were different relaxivities at pH 7.4 and different rates of dissolution after exposure to acidic buffer solutions. The coating structure was a factor in the rate of dissolution of coated MnO nanoparticles and the initial relaxivity measured at pH 7.4. MSA is a small molecule that is distributed on the surface of MnO nanoparticles in way that does not likely cover the entire particle. Therefore, water and protons are readily accessible to the MnO causing fast dissolution at pH 5. The high relaxivity at pH 7.4 was either due to dissolution of some Mn$^{2+}$ at his pH or accessibility of water to the surface of the particle. Similarly, Pluronic PF127 coats the particles due to hydrophobic interactions and also does not likely fully cover the particles or lead to a dense shell to protect MnO particles. The Pluronic PF127 particles also dissolved rapidly and completely a within 20 min at pH 5. The PMAO and PMAO-PEG coated MnO particles had slower dissolution rates than the Pluorinc or MSA coated particles at pH 5, however, the baseline relaxivity of these particles at pH 7.4 was high (2.42 mm$^{-1}$ sec$^{-1}$ for PMAO and 1.79 mm$^{-1}$ sec$^{-1}$ for PMAO-PEG). This decreased the dynamic range associated with transferring the particles to low pH. Both PMAO and PMAO-PEG form a shell which delays the dissolution of the MnO particles. It is not clear why the pH 7.4 relaxivities were as high as they were. This could be due to some Mn$^{2+}$ dissolving or surface interactions of the particles with water.

In contrast to the other coatings, SiO$_2$ forms a comparably dense and thick shell on the particles, providing best protection for particles. Moreover, due to the porous structure of the silica shell, the protons can still reach the MnO core of the particles actively promoting their dissolution and release of Mn$^{2+}$ ions [26]. As a result, MnO@SiO$_2$ showed time-dependent release of Mn$^{2+}$ at pH 5 with only about a third of the Mn$^{2+}$ released after 20 min and taking about 3 days to fully dissolve. Furthermore, relaxivity at pH 7.4 was the lowest and increased 20 fold after complete dissolution to Mn$^{2+}$. Therefore, MnO@SiO$_2$ nanoparticles had the best overall properties. With excellent colloidal and chemical stability at neutral pH, low relaxivity at pH 7.4 and gradual but complete dissolution of Mn$^{2+}$ in the acidic buffer solution.

The gradual enhancement in contrast measured *in vitro* also occurred *in vivo* as shown in the experiments where MnO@SiO$_2$ was directly injected into the thalamus. This direct injection experiment allowed us to monitor the kinetics of contrast development directly *in vivo*. The particles were presumably endocytosed by brain cells resulting in the release of Mn$^{2+}$ leading to positive contrast. The brain injection experiments also enabled us to test of the released Mn$^{2+}$ behaved similarly to directly injected Mn$^{2+}$. Successful tracing from cortex to thalamus indicates that MnO@SiO$_2$ can also be utilized as a source of Mn$^{2+}$ for neural tracing experiments. Similar results were obtained previously in the brain for a transferrin-Mn chelate that also has low relaxivity at pH 7.4 and releases Mn$^{2+}$ after endocytosis to low pH [19]. The transferrin-Mn has a much lower density of Mn making the MnO@SiO$_2$ much more attractive.

The fact that Fe$_3$O$_4$@SiO$_2$ nanoparticles did not give similar neural tracing results indicates that the contrast monitored at the thalamus after injection of the MnO@SiO$_2$ into the cortex was likely due to transport of Mn$^{2+}$. It is difficult to quantitatively compare the T$_1$ enhancement of Mn$^{2+}$ to the T$_2$* contrast from the iron oxide, however, it can be approximately calculated whether the required amount of iron should have been detected in the thalamus based on the Mn$^{2+}$ results. Using the simple relationship,

$$1/T_{i-observed} = 1/T_{i-initial} + relaxivity^*[contrast\ concentration],$$
$$i = 1\ or\ 2$$

for T$_{1-observed}$ = 1150 ms, T$_{1-initial}$ = 1850 ms and relaxivity = 6.1 s$^{-1}$ mm$^{-1}$, the Mn$^{2+}$ contrast concentration is ∼0.054 mm; however, if we assume a detectable T$_{2-observed}^*$ = 30 ms, T$_{2-initial}^*$ = 35 ms and relaxivity = 92.5 s$^{-1}$ mm$^{-1}$, the required iron oxide contrast concentration would be ∼0.051 mm. The T$_1$ values are estimated from our previous work [13] and T$_2^*$ values are obtained from T$_2^*$-mapping measurements on thalamus (data not shown). This indicates that once we see the T$_1$ contrast enhancement with Mn$^{2+}$, its concentration exceeds 0.054 mm; on the other hand, since we did not see any decrease of contrast when Fe$_3$O$_4$@SiO$_2$ particles were used, we concluded that the iron concentration in the thalamus was below 0.051 mm. This may not exclude the possibility of a small number of particles being transported by the neuronal pathway but they do indicate that the majority of the positive contrast at the thalamus did not comes from transport of MnO@SiO$_2$ but rather dissolved Mn$^{2+}$.

Tracing of neural circuits after injection of Mn$^{2+}$ salts has been widely used and a source of slowly released Mn$^{2+}$ might extend the range of tracing experiments that can be performed. While contrast took more time to develop at the brain injection site with MnO@SiO$_2$ as compared to MnCl$_2$, there was no difference in the neuronal tracing results when compared with MnCl$_2$ [13]. The time scale of tracing (a few hours) is much longer than the dissolution time of particles resulting in similar neural tracing. A particle coating that delayed dissolution for hours would be useful to modify the tracing properties.

MnO@SiO$_2$ nanoparticles were infused into mice body via the tail vein to determine the contrast properties in the body. This is important if future work is geared to using the particles to target specific receptors or cell types. The blood half-life of the particles was about 10 min. This means that the slow dissolution (half time of about 6−8 h) of the particles is longer than the blood time. This enables particles to be targeted and there is time for washout of non-specific interactions long before maximal enhancements would occur. There was a fast component of dissolution leading to about 1/3 of the MnO to be dissolved within 20 min which is on the order of the blood half-life. Eliminating this fast component of dissolution would mean contrast would develop on a time scale much longer than the blood half-life.

The results of $T_1$-weighted contrast increase in a variety of tissues were consistent with low uptake MnO@SiO$_2$ by most of the tissues measured. Surprisingly, there was a large increase in contrast in the gallbladder. The gallbladder is not known to accumulate nanoparticles. This combined with the fact that enhancement of the gallbladder began later than the liver, led to a model that Kupffer cells in the liver actively uptake the particles and that dissolved Mn$^{2+}$ is transported from the liver through bile to the gallbladder. To determine whether SiO$_2$ coated particles directly target the gallbladder, Fe$_3$O$_4$@SiO$_2$ nanoparticles were injected IV and $T_2$-weighted MRI was performed. In contrast to the MnO@SiO$_2$ particles, the Fe$_3$O$_4$@SiO$_2$ nanoparticles accumulated in the liver but not the gallbladder. Thus it is likely that the MnO@SiO$_2$, are first endocytosed by liver cells, the particles then dissolve resulting in Mn$^{2+}$ release. The Mn$^{2+}$ ions are then excreted through bile duct leading to the positive contrast in the gallbladder. This is an interesting process that may be useful for imaging liver function and direct imaging of the gallbladder.

Both the brain tracing and the liver to gallbladder transfer of dissolved Mn$^{2+}$ points to a strength and weakness of the MnO@SiO$_2$ particles. The release of Mn$^{2+}$ at low pH greatly increases relaxivity and the ability of Mn$^{2+}$ to leave endosomes/lysosomes enables an increase the volume distribution of the agent further enhancing sensitivity. However, the ability of Mn$^{2+}$ to be transported by different mechanisms to sites remote from where the particles enter means care has to be taken to distinguish the site of entry of MnO@SiO$_2$ particles and the site of contrast measured by MRI. The ability of Mn$^{2+}$ to transport opens the interesting possibility of using the particles to make functional measurements of tissue as was the case for liver transport to gallbladder. Indeed one can imagine a mixed MnO/Fe$_3$O$_4$ particle that would enable direct detection of the particles along with transport of the Mn$^{2+}$.

## 5. Conclusions

MnO@SiO$_2$ nanoparticles have demonstrated excellent properties of low MRI $T_1$ relaxivity at pH 7.4, a large increase in relaxivity at pH 5 due to slow and complete dissolution to Mn$^{2+}$. Indeed there was a 20 fold change in relaxivity from pH 7.4 to pH 5. The in vitro properties of these novel particles were verified in vivo with direct injections into brain and intravenous injections. The rate of dissolution was slowed by the SiO$_2$ coat to be longer than the blood half-life enabling particles that have not specifically been taken up by target cells to clear on the order of the development of MRI contrast. The slow release of MRI contrast triggered by the low pH environment of the endosomal/lysosomal pathway should be very useful for development of molecular imaging agents with improved sensitivity and specificity.

## Acknowledgements

## References

[1] Lin YJ, Koretsky AP. Manganese ion enhances T1-weighted MRI during brain activation: an approach to direct imaging of brain function. Magn Reson Med 1997;38:378–88.

[2] Caravan P, Ellison JJ, McMurry TJ, Lauffer RB. Gadolinium(III) chelates as MRI contrast agents: structure, dynamics, and applications. Chem Rev 1999;99:2293–352.

[3] Louie AY, Huber MM, Ahrens ET, Rothbacher U, Moats R, Jacobs RE, et al. In vivo visualization of gene expression using magnetic resonance imaging. Nat Biotech 2000;18:321–5.

[4] Li WH, Fraser SE, Meade TJ. A calcium-sensitive magnetic resonance imaging contrast agent. J Am Chem Soc 1999;121:1413–4.

[5] Zhang SR, Trokowski R, Sherry AD. A paramagnetic CEST agent for imaging glucose by MRI. J Am Chem Soc 2003;125:15288–9.

[6] Lelyveld VS, Brustad E, Arnold FH, Jasanoff A. Metal-substituted protein MRI contrast agents engineered for enhanced relaxivity and ligand sensitivity. J Am Chem Soc 2011;133:649–51.

[7] Krishnan KM. Biomedical nanomagnetics: a spin through possibilities in imaging, diagnostics, and therapy. IEEE Trans Mag 2010;46:2523–58.

[8] Park IK, Ng CP, Wang J, Chu B, Yuan C, Zhang S, et al. Determination of nanoparticle vehicle unpackaging by MR imaging of a T2 magnetic relaxation switch. Biomaterials 2008;29:724–32.

[9] Taktak S, Sosnovik D, Cima MJ, Weissleder R, Josephson L. Multiparameter magnetic relaxation switch assays. Anal Chem 2007;79:8863–9.

[10] Atanasijevic T, Shusteff M, Fam P, Jasanoff A. Calcium-sensitive MRI contrast agents based on superparamagnetic iron oxide nanoparticles and calmodulin. PNAS 2006;103:14707–12.

[11] Koretsky AP, Silva AC. Manganese-enhanced magnetic resonance imaging (MEMRI). NMR Biomed 2004;17:527–31.

[12] Silva AC, Lee JH, Aoki L, Koretsky AR. Manganese-enhanced magnetic resonance imaging (MEMRI): methodological and practical considerations. NMR Biomed 2004;17:532–43.

[13] Tucciarone J, Chuang KH, Dodd SJ, Silva A, Pelled G, Koretsky AP. Layer specific tracing of corticocortical and thalamocortical connectivity in the rodent using manganese enhanced MRI. Neuroimage 2009;44:923–31.

[14] Hu TCC, Christian TF, Aletras AH, Taylor JL, Koretsky AP, Arai AE. Manganese enhanced magnetic resonance imaging of normal and ischemic canine heart. Magn Reson Med 2005;54:196–200.

[15] Leoni L, Serai SD, Magin RL, Roman BB. Functional MRI characterization of isolated human islet activation. NMR Biomed 2010;23:1158–65.

[16] Na HB, Lee JH, An KJ, Park YI, Park M, Lee IS, et al. Development of a T1 contrast agent for magnetic resonance imaging using MnO nanoparticles. Angew Chem-Int Edit 2007;46:5397–401.

[17] Shapiro EM, Koretsky AP. Convertible manganese contrast for molecular and cellular MRI. Magn Reson Med 2008;60:265–9.

[18] Bennewitz MF, Lobo TL, Nkansah MK, Ulas G, Brudvig GW, Shapiro EM. Biocompatible and pH-sensitive PLGA encapsulated MnO nanocrystals for molecular and cellular MRI. ACS Nano 2011;5:3438–46.

[19] Sotak CH, Sharer K, Koretsky AP. Manganese cell labeling of murine hepatocytes using manganese(III)-transferrin. Contrast Media Mol 2008;3:95–105.

[20] Kabanov AV, Batrakova EV, Alakhov VY. Pluronic((R)) block copolymers for overcoming drug resistance in cancer. Adv Drug Deliver Rev 2002;54:759–79.

[21] Lee YC, Pakhomov AB, Krishnan KM. Size-driven magnetic transitions in monodisperse MnO nanocrystals. J Appl Phys 2010;107:09E124.

[22] Chatterji T, Su YX, Iles GN, Lee YC, Khandhar AP, Krishnan KM. Antiferromagnetic spin correlations in MnO nanoparticles. J Magn Magn Mater 2010;322:3333–6.

[23] Park J, Kang EA, Bae CJ, Park JG, Noh HJ, Kim JY, et al. Synthesis, characterization, and magnetic properties of uniform-sized MnO nanospheres and nanorods. J Phys Chem B 2004;108:13594–8.

[24] Gonzales M, Krishnan KM. Synthesis of magnetoliposomes with monodisperse iron oxide nanocrystal cores for hyperthermia. J Magn Magn Mater 2005;293:265–70.

[25] Paxinos G, Waston C. The rat brain in stereotaxic coordinates. 5th ed. San Diego (CA): Acdemic Press; 2005.

[26] Tago T, Shibata Y, Hatsuta T, Miyajima K, Kishida M, Tashiro S, et al. Synthesis of silica-coated rhodium nanoparticles in reversed micellar solution. J Mater Sci 2002;37:977–82.

[27] Corot C, Robert P, Idee JM, Port M. Recent advances in iron oxide nanocrystal technology for medical imaging. Adv Drug Deliver Rev 2006;58:1471–504.